Available online at www.sciencedirect.com
SCIENCE DIRECT®
Journal of Magnetic Resonance 174 (2005) 279–286
JMR Journal of Magnetic Resonance
www.elsevier.com/locate/jmr

# Image artifacts in very low magnetic field MRI: The role of concomitant gradients

Dmitriy A. Yablonskiy [a,b,*], Alexander L. Sukstanskii [a], Joseph J.H. Ackerman [a,c,d]

[a] Department of Radiology, Washington University, One Brooking Drive, St. Louis, MO 63130, USA
[b] Department of Physics, Washington University, One Brooking Drive, St. Louis, MO 63130, USA
[c] Department of Chemistry, Washington University, One Brooking Drive, St. Louis, MO 63130, USA
[d] Department of Internal Medicine, Washington University, One Brooking Drive, St. Louis, MO 63130, USA

Received 1 November 2004; revised 16 February 2005
Available online 17 March 2005

**Abstract**

While MRI at very low magnetic fields has certain potential advantages, it may also face problems that are not typical for MRI at conventional and high field (0.1–10 T). Major differences arise due to the presence of concomitant components of inhomogeneous magnetic field (gradients) that are transverse to the major $B_z$ field, $B_0$. These concomitant transverse field components are inevitably generated by the same gradient coils that generate desired $B_z$ imaging gradients as routinely used in MRI for spatial encoding. In the hypothetical case (linear spatial variation of $B_z$ field amplitude due to the imaging gradients, no concomitant transverse field components, no $B_0$ and $B_1$ field inhomogeneities, etc.), Fourier transform MRI preserves the shape of the real object being examined. It is demonstrated herein that unavoidable concomitant transverse field gradients, $G$, result in an image deformation of the object's actual shape by bending straight lines and planes with a characteristic curvature radius $R_c = B_0/G$. For imaging gradients on the order of 10 mT/m and $B_0$ of 1 T, the radius $R_c$ is about 100 m and image distortions are generally negligible. However, for $B_0$ of 1 mT, $R_c$ is 10 cm, which is less than a typical FOV in human studies. This manuscript derives expressions describing geometrical relationships between the imaged object and the obtained MR data. In addition to geometrical distortions, image intensity will be modulated in a complex, spatially dependent manner. Hence, if unaccounted for, corresponding image distortions—geometry and intensity—will create substantial difficulties in very low field image interpretation.


*Keywords:* MRI; Low magnetic field; Concomitant gradient; Maxwell term; Imaging with hyperpolarized gases

## 1. Introduction

The introduction of hyperpolarized gases by Happer [1] and the advent of MR imaging of these gases in biological settings demonstrated by Albert et al. [2] has led to increasing interest in MRI with hyperpolarized gases (see, for example, [3,4]). Because the imaged gas is already pre-polarized to about 10–50% of its maximal achievable polarization, there is no need for a high "polarizing" magnetic field $B_0$ to attain a strong MR signal. This fact was quickly realized and successful attempts were made to build MRI apparatus for imaging hyperpolarized gases at the very low magnetic fields of several mT [5–8]. While MRI at very low magnetic fields has certain potential advantages, it may also face problems that are not typical for MRI at conventional and high field (0.1–10 T). This paper is concerned with one set of these problems—artifacts resulting from concomitant magnetic field gradients created by the gradient coils, which are used to encode spatial information in magnetic resonance imaging. Maxwell's equations predict that coils generating gradients $\partial B_z/\partial x$, $\partial B_z/\partial y$, and

* Corresponding author. Present address: Mallinckrodt Institute of Radiology, Campus Box 8227, Washington University School of Medicine, 660 S. Euclid Ave., St. Louis, MO 63110, USA. Fax: +1 314 362 0526.
*E-mail address:* YablonskiyD@wustl.edu (D.A. Yablonskiy).

1090-7807/$ - see front matter © 2005 Elsevier Inc. All rights reserved.
doi:10.1016/j.jmr.2005.02.016

$\partial B_z/\partial z$ will always generate gradients of transverse components of magnetic field such as $\partial B_x/\partial z$, $\partial B_y/\partial z$, $\partial B_x/\partial x$, and $\partial B_y/\partial y$, as first pointed out in MRI literature by Norris and Hutchison [9]. These gradients have the same amplitude as $B_z$ gradients produced by the same coil. Gradients as strong as 10–20 mT/m are typically used in human imaging experiments. Hence, transverse magnetic fields as strong as 5–10 mT will also be present (FOV about 0.5 m). These so-called "concomitant" magnetic fields are known to create a number of artifacts even in MRI at the conventional magnetic field of 1.5 T, especially in imaging methods sensitive to signal phase evolution, such as EPI and phase contrast MRI techniques for flow quantification [10–13]. However, for most MRI techniques at conventional magnetic fields, the concomitant fields do not impose significant problems as the effective magnetic field defining the Larmor frequency differs only slightly from $B_z$. However, in a very low field scanner (several mT or even μT), the transverse concomitant magnetic field created by the gradients may be on the order of or even larger then $B_0$. This will create substantial artifacts in the imaging experiment. A similar problem will exist for imaging in the Earth's magnetic field [14]. Such artifacts will be most pronounced in MRI at micro-Tesla fields [15,16].

Fourier MRI provides transformation of the imaged object into a digital image. In a hypothetical case (spatial linear variation of $B_z$ field amplitude due to imaging gradients, no concomitant field gradients, no $B_0$ and $B_1$ field inhomogeneities, etc.), this results in an angle-preserving transformation (preserves shapes of the objects). For example, in 2D FT MRI (gradient recalled or spin echo), a selected plane in the object corresponds to a plane in the image, parallel, and orthogonal lines in the object correspond to parallel and orthogonal lines in the image, etc. It is shown herein that the unavoidable presence of concomitant gradients, $G$, deforms this transformation by bending straight lines and planes. The characteristic length scale describing this deviation from linearity (curvature radius $R_c$) and a characteristic parameter $\varepsilon$ defining resulting deformations in the image are

$$\varepsilon = R_c/L, \quad R_c = B_0/G, \tag{1}$$

where $L$ is the image field of view (FOV). For imaging gradients on the order of 10 mT/m and $B_0$ of 1 T, $R_c$ is 100 m and image distortions are generally negligible. However, for $B_0 \sim 1$ mT, $R_c \sim 10$ cm, which is less than a typical FOV in human studies. Hence, corresponding image distortions will create substantial difficulties in image interpretation if unrecognized. Interestingly, imaging at conventional magnetic fields with ultra high amplitude gradients may also be prone to such image distortions. For example, $R_c$ approaches 10 cm for $B_0 \sim 1$ T and gradient $G \sim 10$ T/m (1000 G/cm), a gradient amplitude already available with specialized imaging devices.

## 2. Imaging gradients

Magnetic field gradients are broadly used in MRI for different purposes: slice selection, phase, and frequency encoding, etc. We will consider these procedures separately but we first discuss the concomitant magnetic field and gradient ramping.

### 2.1. Concomitant magnetic field (Maxwell terms)

Any static magnetic field $\mathbf{b}(\mathbf{r})$ in a free space satisfies Maxwell's equations

$$\nabla \cdot \mathbf{b}(\mathbf{r}) = 0, \quad \nabla \times \mathbf{b}(\mathbf{r}) = 0, \tag{2}$$

from which it immediately follows that an inhomogeneous magnetic field cannot have a single non-zero component. In the general case, if a desired ($Z$-axis) inhomogeneous magnetic field

$$b_z = G_x x + G_y y + G_z z \tag{3}$$

created by gradient coils is applied during an imaging experiment, the total actual magnetic field present in the MR scanner will also include concomitant inhomogeneous components $b_x$ and $b_y$:

$$\mathbf{B} = b_x \mathbf{e}_x + b_y \mathbf{e}_y + (B_0 + b_z)\mathbf{e}_z, \tag{4}$$

where [10]

$$b_x = -\alpha G_z x + G_x z, \quad b_y = (\alpha - 1) G_z y + G_y z, \tag{5}$$

where $\mathbf{e}_x$, $\mathbf{e}_y$, and $\mathbf{e}_z$ are unit vectors in transverse $(x, y)$ and longitudinal ($z$) directions (defined with respect to the main magnetic field $\mathbf{B}_0$ direction), and parameter $\alpha$ depends on the specific gradient coil design (for the $z$-gradient with cylindrical symmetry, $\alpha = 1/2$). The presence of an imaged object in the scanner only slightly modifies Eqs. (4) and (5) since magnetic susceptibility of most biological tissues is very small, on the order of 1 ppm.

### 2.2. Gradient ramping effects

If the characteristic period $\tau_r$ required to ramp-up or ramp-down the magnetic field gradient is longer than the inverse of the Larmor frequency, $\gamma B_0 \tau_r \gg 1$, then nuclear spins will be in the adiabatic regime [17] correspondingly adjusting their orientation with respect to the changing magnetic field direction and amplitude. In the alternative case, $\gamma B_0 \tau_r \ll 1$, turning gradients on and off may be considered an instantaneous (non-adiabatic) process. Hence, net spin orientation does not change during the gradient ramp period. Following a gradient ramp period, spins immediately start to precess about the new total local magnetic field direction, Eq. (4). For imaging in a 1 mT field, a gradient ramp period of about 25 μs or longer is sufficient to satisfy the adiabatic condition. However, imaging in a 1 μT field

requires a gradient ramp period of about 25 ms or longer to satisfy the adiabatic condition. Obviously, the adiabatic condition holds for magnetic fields of 1 mT and higher for most existing field gradient systems. However, at very low micro-Tesla fields the fast switching (non-adiabatic) regime can be readily achieved with consequences likely to be undesired, vide infra.

In both the cases (adiabatic and fast switching regime), the local Larmor angular frequency $\omega$ in the presence of a gradient field (4) is equal to

$$\omega = \gamma\left[(B_0 + b_z)^2 + (b_x)^2 + (b_y)^2\right]^{1/2}, \tag{6}$$

where longitudinal and transverse components of gradient-originated magnetic field are defined by Eqs. (3) and (5). In the adiabatic regime, if the starting orientation of nuclear magnetization is along $\mathbf{B}_0$, during a gradient ramp period the net spin orientation will continually align along the total local magnetic field direction as this direction evolves during application of the gradient ramp, Eq. (4). Hence, by the end of a ramp-up period, the nuclear magnetization will be aligned along the new direction of the local magnetic field $\mathbf{B}$, Eq. (4), in the adiabatic regime. It will remain, however, aligned along the $\mathbf{B}_0$ direction in the fast switching regime. If the starting orientation of nuclear magnetization is tilted from $\mathbf{B}_0$ (following an RF pulse, for example), the axis of the cone of nuclear spin precession will follow $\mathbf{B}$ in adiabatic regime and will remain unaltered in the case of fast switching gradients. In the former case, during a gradient ramp period $\tau_r$ the spins will accumulate an additional spatially inhomogeneous phase

$$\Delta\varphi = \int_0^{\tau_r} \omega(t)\,\mathrm{d}t, \tag{7}$$

where the temporal dependence of local frequency depends upon that of the local magnetic field during the ramp period according to Eq. (6).

Note that generally speaking, the tissue relaxation processes might affect the above consideration if the gradient ramp time $\tau_r$ is comparable or longer than the $T_1$, $T_2$ or $T_2^*$ tissue relaxation time constants.

## 3. Slice selection procedure

### 3.1. Axial slice selection gradients

Let us start with the slice selection, for example, along the direction $x$ perpendicular to the main field $\mathbf{B}_0$. For this purpose, a field with a gradient $b_z = G_x x$ is usually applied. Such a field is necessarily accompanied by the concomitant field $b_x = G_x z$ (5). The total magnetic field $B(x,z)$ determining the local Larmor frequency $\omega(x,z) = \gamma B(x,z)$ is equal to

$$B(x,z) = |\mathbf{B}(x,z)| = \left[(B_0 + G_x x)^2 + (G_x z)^2\right]^{1/2}. \tag{8}$$

If the concomitant field $G_x z$ is ignored, a RF pulse selecting frequency $\omega$ excites spins along a plane $x = x_0$, where $x_0$ satisfies the condition

$$\gamma(B_0 + G_x x_0) = \omega. \tag{9}$$

However, accounting for the concomitant field, the RF pulse selecting the same frequency excites spins with coordinates satisfying the condition

$$\gamma\left[(B_0 + G_x x)^2 + (G_x z)^2\right]^{1/2} = \omega. \tag{10}$$

Consequently, a cylindrical surface

$$(x - x_c)^2 + z^2 = R_x^2, \quad R_x = |x_0 + B_0/G_x|, \quad x_c = -B_0/G_x \tag{11}$$

is excited rather than the plane $x = x_0$ (9). This cylinder has an axis parallel to the $Y$-axis crossing through the point $\{x_c = -B_0/G_x, 0, 0\}$ and has a radius $R_x$ (11). The "targeted" plane $x = x_0$ is tangential to the cylinder. Note also that the position of the cylinder's axis is independent of $x_0$, i.e., independent of the RF slice-selection frequency $\omega$ (9). Thus, RF pulses with different frequencies excite not a set of parallel planes but a set of *concentric* cylinders of different radii. As a result, a targeted slice of a thickness $\Delta x$ "deforms" into an annulus between two cylinders; a cross-section of this annulus being a ring of the same thickness $\Delta x$, as shown in Fig. 1.

The deviation of the points on the cylinder's surface (11) from the targeted plane $x = x_0$, $\delta x = x - x_0$, de-

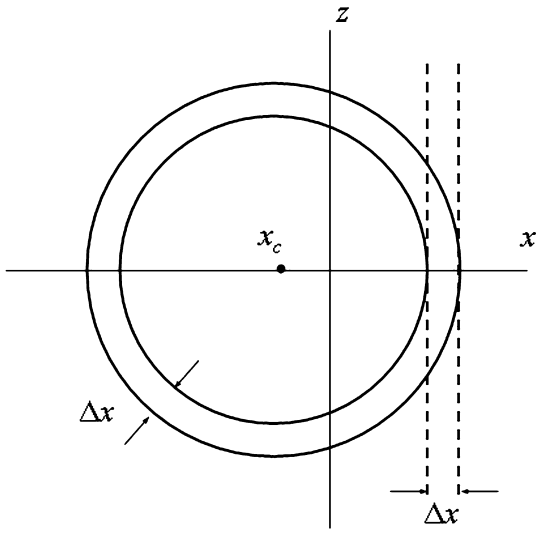


Fig. 1. A cross-section of a slice selected by RF pulse and the field gradient $b_z = G_x x$ with accounting for the concomitant filed $b_x = G_x z$ (solid lines). The targeted slice, i.e., slice that would be selected by the same gradient if the concomitant filed was not present (hypothetical, unrealizable ease), is shown by dashed lines.

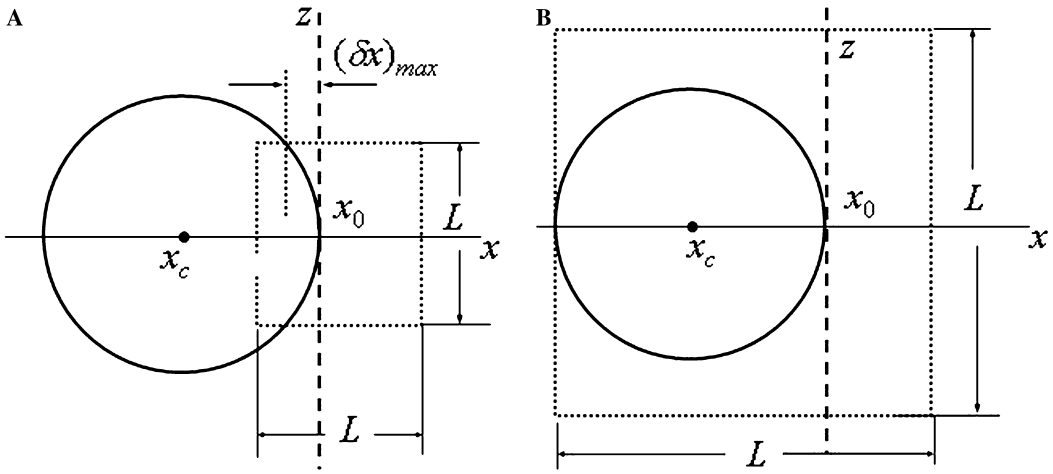


Fig. 2. A cross-section of the cylinder selected by the field gradient $b_z = G_x x$ with accounting for the concomitant field $b_x = G_x z$. The FOV of dimension $L$ is shown by dashed square. (A) $\varepsilon = G_x L/B_0 \ll 1$, the maximal deviation $(\delta x)_{\max} \simeq \varepsilon L/8 \ll L$ being achieved at $|z| \sim L/2$. (B) $\varepsilon = 4$.

pends on their $z$-coordinate. If the field $B_0$ is strong enough and the distortion parameter $\varepsilon = G_x L/B_0$ (1) is small, the radius $R_x \sim B_0/G_x \gg L$, and only a small portion of the circle resides within the FOV. In this case (Fig. 2A), the maximal deviation $(\delta x)_{\max}$ achieved at the edge of the FOV at $|z| \sim L/2$ is also small as compared to the FOV,$(\delta x)_{\max} \simeq \varepsilon L/8 \ll L$. In this case, the effect of the concomitant fields on a position of spins excited by the RF pulse is small. However, if the field $B_0$ is small enough and $\varepsilon \sim 1$, the situation is different. For example, if $\varepsilon = 4$ the entire circle resides within the FOV (Fig. 2B).

The situation with plane selection along the $Y$-axis is similar to the $X$-axis. To get corresponding results, in all above-derived equations one should substitute $x$ by $y$.

### 3.2. Longitudinal slice-selection gradients

Consider now slice selection along the $Z$-axis. For this case, a field $b_z = G_z z$ is usually applied. Such a field is accompanied by concomitant field components $b_x = -\alpha G_z x$ and $b_y = (1-\alpha) G_z y$ (5). As a result, a targeted plane $z = z_0$ that would be excited by a RF pulse with slice-selection frequency $\omega$,

$$\gamma(B_0 + G z_0) = \omega, \tag{12}$$

in a hypothetical case without concomitant gradients, transforms into an ellipsoid given by

$$\alpha^2 x^2 + (1-\alpha)^2 y^2 + (z - z_c)^2 = R_z^2, \tag{13}$$

where

$$z_c = -B_0/G_z, \quad R_z = |z_0 - z_c|. \tag{14}$$

For gradient coils symmetric about the $Z$-axis, $\alpha = 1/2$, Eq. (13) describes an ellipsoid of revolution with the half-axes $(2R, 2R, R)$. If the slice-selection gradient amplitude is held constant, different slice-selection frequencies will result in a set of ellipsoids with the same center point $(0, 0, z_c = -B_0/G_z)$. The entire space can be filled by ellipsoids with different $R_z$ (14) corresponding to different $\omega$ and hence different positions of the targeted plane $z = z_0$. In short, the slice selection procedure results in ellipsoid-like slices rather than simple plane-parallel slices.

All the above discussion was devoted to "geometrical" aspects of the slice selection procedure. It should be noted that the presence of concomitant fields will also lead to an inhomogeneous distribution of magnetization in the selected slice. For example, if the slice-selecting gradient were turned on instantly (fast switching regime) just prior to turning on the RF pulse, the spins would precess in the presence of both the RF field and the transverse component of the concomitant field. This will lead to a rather complex and spatially dependent distribution of magnetization orientation, thus ultimately signal intensity, within the selected curved slice. In the adiabatic case, by the end of the ramp-up period, spins will align along the direction of magnetic field (4). Since this field is inhomogeneous in both magnitude and orientation, the following slice-selecting RF pulse will also create a rather complex and spatially dependent distribution of magnetization orientation, thus ultimately signal intensity, within the selected curved slice. A detail description of this phenomenon is beyond the scope of the manuscript.

## 4. Frequency encoding (read-out) procedure

### 4.1. Transverse read-out gradients

Consider first the read-out procedure with the read-out gradient in the $X$-direction $b_z = G_x x$ leading to the corresponding concomitant field $b_x = G_x z$. The total

magnetic field lies in the $XZ$ plane and makes a position-dependent angle $\beta$ with the axis $Z$,

$$\tan\beta = G_x z/(B_0 + G_x x). \tag{15}$$

In the presence of the read-out gradient, spins initially oriented in the $XY$-plane precess about the local net magnetic field $\mathbf{B}$ (4) with a frequency

$$\omega = \gamma\left[(B_0 + G_x x)^2 + (G_x z)^2\right]^{1/2}. \tag{16}$$

In the fast switching regime, precession during the time $t$ of magnetization initially oriented in the $XY$ plane with the angle $\varphi_0$ with the $X$-axis, will result in the following distribution of magnetization:

$$\begin{aligned} M_x(x,z;t) =& M_0[\cos\varphi_0 \cdot \left(\cos^2\beta \cdot \cos\omega t + \sin^2\beta\right) \\ & - \sin\varphi_0 \cdot \cos\beta \cdot \sin\omega t], \\ M_y(x,z;t) =& M_0(\sin\varphi_0 \cdot \cos\omega t \\ & + \cos\varphi_0 \cdot \cos\beta \cdot \sin\omega t), \\ M_z(x,z;t) =& M_0 \sin\beta \cdot [\cos\beta \cdot \cos\varphi_0 \cdot (1 - \cos\omega t) \\ & + \sin\varphi_0 \cdot \sin\omega t], \end{aligned} \tag{17}$$

where both the angle $\beta$ and the Larmor frequency $\omega$ depend on $x$ and $z$ according to Eqs. (15) and (16). In the adiabatic case, expression for magnetization will be only slightly different from Eqs. (17) because phase accumulation (7) during the ramp-up period should be taken into account.

In the limit $B_0 \gg G_x L$ ($\varepsilon \ll 1$), the role of the concomitant gradients is negligible: the angle $\beta = 0$, the magnetization $\mathbf{M}$ remains in the $XY$ plane and is given by a standard expression

$$\begin{aligned} M_+(x,z;t) &= M_+(x;t) = M_x(x;t) + \mathrm{i}M_y(x;t) \\ &= M_0 \exp\left[\mathrm{i}(\gamma B_0 t + \varphi_0)\right] \cdot \exp\left(\mathrm{i}\gamma G_x x t\right). \end{aligned} \tag{18}$$

As usually, surfaces of constant frequency in this case correspond to planes $x = x_0$ with $x_0$ determined from the equation

$$\gamma(B_0 + G_x x_0) = \omega. \tag{19}$$

However, if the concomitant field is taken into account, hence $\beta \neq 0$, surfaces of constant frequency become cylinders:

$$(x - x_c)^2 + z^2 = R_x^2, \quad x_c = -B_0/G_x, \quad R_x = |\omega/\gamma G_x| \tag{20}$$

rather than planes $x = x_0$ (19). Note that the cylinders (20) are tangential to planes (19). Geometrically, the situation is similar to the slice selection procedure and can be illustrated by figures practically identical to Figs. 1 and 2. A maximal deviation of the cylinder from the plane $x = x_0$ within the FOV is about

$$(\delta x)_{\max} \simeq \varepsilon L/8. \tag{21}$$

In the case of a small gradient, $G_x \ll B_0/L$, $(\delta x)_{\max} \ll L$ and becomes $\sim L$ for $\varepsilon \sim 1$.

The situation with the read-out gradient along the $Y$-axis is similar to the $X$-axis. To get corresponding results, in all above-derived equations one should substitute $x$ by $y$.

### 4.2. Longitudinal read-out gradients

If the read-out gradient is applied along the $Z$-axis, surfaces of constant frequency are ellipsoids

$$\begin{aligned} &\alpha^2 x^2 + (1-\alpha)^2 y^2 + (z - z_c)^2 = R_z^2, \\ &z_c = -B_0/G_z, \quad R_z = |\omega/\gamma G_z|. \end{aligned} \tag{22}$$

All the ellipsoids have the same center at the point $(0, 0, z_c = -B_0/G_z)$ and the entire space can be filled by the ellipsoids with different $R_z$ (22) corresponding to different $\omega$ and hence different positions of the targeted plane $z = z_0$ designated by the equation

$$\gamma(B_0 + G_z z_0) = \omega. \tag{23}$$

In short, the read-out procedure results in ellipsoid-like surfaces rather than simple plane-parallel surfaces.

## 5. Phase encoding procedure

Consider, for example, a phase encoding procedure with the encoding gradient applied along the $Y$-axis, $b_z = G_y y$. The encoding gradient is accompanied by the concomitant field $b_y = G_y z$. The total magnetic field $\mathbf{B}$ is now in the $YZ$ plane and makes an angle $\beta$ with the axis $Z$:

$$\tan\beta = G_y z/(B_0 + G_y y). \tag{24}$$

Let us also suppose that, after excitation by the RF pulse, the spin magnetization vector $\mathbf{M}$ was oriented in the plane $XY$ making an angle $\varphi_0$ with the Cartesian axis $X$: $\mathbf{M}(0) = M_0\ (\cos\varphi_0, \sin\varphi_0, 0)$. Under the influence of the magnetic field $\mathbf{B}$, the magnetization $\mathbf{M}$ starts to rotate about the vector $\mathbf{B}$ with the Larmor frequency

$$\omega = \gamma|\mathbf{B}| = \gamma\left[(B_0 + G_y y)^2 + (G_y z)^2\right]^{1/2}. \tag{25}$$

In the adiabatic regime, this leads to a phase accumulation over the phase encoding period $\tau$,

$$\Delta\varphi = \int_0^\tau \omega(t)\,\mathrm{d}t, \tag{26}$$

where the frequency (25) depends on the time through the gradient time dependence. After the phase encoding, the magnetization $\mathbf{M}$ returns to the $XY$ plane and is given by an expression

$$\begin{aligned} M_+(y,z;\tau) &= M_x(y,z;\tau) + \mathrm{i}M_y(y,z;\tau) \\ &= M_0 \cdot \exp(\mathrm{i}(\varphi_0 + \Delta\varphi)). \end{aligned} \tag{27}$$

In case of short ramp periods (but still within adiabatic regime) compared to the duration of phase-encoding gradient $\tau$, the phase accumulation (26) reduces to

$$\Delta\varphi = \gamma\left[(B_0 + G_y y)^2 + (G_y z)^2\right]^{1/2}\tau. \quad (28)$$

Even in this case the phase dependence on spin position is no longer linear.

If the concomitant fields are ignored, the magnetization **M** is given by a standard expression

$$\begin{aligned} M_+(y,z;\tau) &= M_+(y;\tau) = M_x(y;\tau) + \mathrm{i}M_y(y;\tau) \\ &= M_0 \exp\left[\mathrm{i}(\gamma B_0\tau + \varphi_0)\right] \cdot \exp\left(\mathrm{i}\gamma G_y y\tau\right). \end{aligned} \quad (29)$$

As usual, in this case surfaces of constant phase correspond to planes $y = y_0$ with $y_0$ determined from the equation

$$\gamma G_y y_0 \tau = \varphi. \quad (30)$$

However, if the concomitant fields are taken into account, these targeted planes transform to cylinders in the same manner as described in the previous sections (slice-selection and read-out encoding). Correspondingly, in the case of phase-encoding gradients applied along $Z$ direction, the targeted planes transform to ellipsoids.

The situation is even more complicated in the fast switching regime. Indeed, during the gradient pulse period $\tau$, the spins originally in $XY$ plane, turn through an angle $\omega\tau$ about the vector **B**. It is easy to verify that after this rotation, the components of the spin's magnetization vector are given by

$$\begin{aligned} M_x(y,z;\tau) &= M_0(\cos\varphi_0 \cdot \cos\omega\tau - \sin\varphi_0 \cdot \cos\beta \cdot \sin\omega\tau), \\ M_y(y,z;\tau) &= M_0[\sin\varphi_0 \cdot (\cos^2\beta \cdot \cos\omega\tau + \sin^2\beta) \\ &\quad + \cos\varphi_0 \cdot \cos\beta \cdot \sin\omega\tau], \\ M_z(y,z;\tau) &= M_0 \sin\beta \cdot [\cos\beta \cdot \sin\varphi_0 \cdot (1 - \cos\omega\tau) \\ &\quad - \cos\varphi_0 \cdot \sin\omega\tau]. \end{aligned} \quad (31)$$

First, a spatially inhomogeneous $z$-component of **M** appears, Eq. (31); second, an absolute value of the projection of **M** on the $XY$-plane also depends on the position; third, a phase formally defined as $\varphi = \tan^{-1}(M_y/M_x)$ is now not a plane $y = y_0$ but rather a complicated curve surface. In the particular case, $\varphi_0 = 0$, this surface is described by the equation

$$\cos\beta(y,z) \cdot \tan(\omega(y,z)\tau) = \tan\varphi, \quad (32)$$

where both the angle $\beta$ and the Larmor frequency $\omega$ depend on $y$ and $z$ according to Eqs. (24) and (25). It is easy to see that surfaces of a constant $\omega$ are cylinders with a common axis along the line $\mathbf{r} = \{x, -B_0/G_y, 0\}$ parallel to the $X$-axis. Surfaces of constant angle $\beta$ are planes passing the same line $\mathbf{r} = \{x, -B_0/G_y, 0\}$. However, the geometry of the surfaces of constant phase $\varphi$, even in a simple case $\varphi_0 = 0$, Eq. (32), is rather complicated and, therefore, to follow how the phase encoding gradient has encoded the spins by their transverse phases is cumbersome and almost impractical.

## 6. Gradients as excitation pulses

Another important feature of MR imaging at very low fields arises from gradient pulses in the fast switching regime acting as "excitation pulses." Indeed, the presence of the applied gradient results in an effective magnetic field, due to the presence of concomitant fields, which is tilted from the original $\mathbf{B}_0$ direction. This leads to precession of the local magnetization vector about the new tilted field. Consider, for example, a magnetization vector originally oriented along the $Z$-axis and which experiences an instantly applied gradient pulse $b_z = G_y y$ of duration $\tau$. The corresponding concomitant field is $b_y = G_y z$. During the period $\tau$, the magnetization vector will rotate with the frequency $\omega$, Eq. (25), to a new spatial-dependent orientation:

$$\begin{aligned} M_x(\tau) &= M_0 \sin\beta \cdot \sin\omega\tau, \\ M_z(\tau) &= M_0(\sin^2\beta \cdot \cos\omega\tau + \cos^2\beta), \\ M_y(\tau) &= M_0 \sin\beta \cdot \cos\beta \cdot (1 - \cos\omega\tau), \end{aligned} \quad (33)$$

where $\tan\beta = G_y z/(B_0 + G_y y)$. Hence, even a gradient without RF pulse will create an inhomogeneous magnetization both longitudinal, $M_z$, and transverse, $M_x$, $M_y$. After switching the gradient off, this inhomogeneous magnetization will precess about $\mathbf{B}_0$ and generate an MR signal. Obviously, the tilt angle is inhomogeneous in space with the maximum value achieved at the edges of FOV, proportional to parameter $\varepsilon$.

## 7. Discussion

Several points should be re-emphasized regarding potential problems that arise in very low field MRI. All these problems relate to the presence of concomitant transverse components of inhomogeneous magnetic field that appear as a result of application of imaging gradients used in MRI for spatial encoding. These concomitant transverse components are *inevitably* generated by the same gradient coils that produce the desired longitudinal imaging components. Longitudinal and concomitant transverse components have the same amplitude.

The presence of concomitant gradients leads to distortion of the similarity relationship between an imaged real object and the resultant images. Standard slice-selection, read-out and phase-encoding procedures identify cylindrical or ellipsoidal surfaces in the object rather than targeted straight planes. Additionally, magnetization is not oriented homogeneously over these surfaces.

An obvious solution to the problems of MRI at very low fields is to use imaging gradients with very low amplitude. In this case, the image deformation parameter $\varepsilon$ (1) can be made small, preserving the accuracy of the image's geometrical parameters. It is instructive to explore this option for the case of imaging the human

lung with hyperpolarized $^3$He gas. The $^3$He lung imaging procedure is typically accomplished during breath-hold period of about 10 s. Due to patient safety and hyperpolarized $^3$He gas availability and cost, generally very few (2–3) breath-holdings measurements are employed during one imaging session. Assume, for this illustration, that one only wants to image the whole lung with a low resolution of 5 mm in-plane and 8 mm slice thickness (actually, one might want to do much better than that). With the FOV of about $40\,\text{cm} \times 40\,\text{cm} \times 20\,\text{cm}$, about 1000 phase-encoding steps are needed, which allows for about 10 ms per step, resulting in less than 5 ms for phase encoding and less than 5 ms for read-out. This requires longitudinal gradient amplitude about 1.5 mT/m, which will create concomitant transverse components resulting in a magnetic field difference of 0.6 mT across the lung. If one is willing to tolerate image distortions no more than 10% ($\varepsilon = 0.4$ according to Eq. (21)), a $B_0$-field of 1.5 mT and higher is required. Further, to reduce the error to 1% would require $B_0$ of at least 15 mT. In general, for a given upper level of image distortion $E$ across a field of view $L$ while employing an imaging gradient of strength $G$, the magnetic field $B_0$ should satisfy condition:

$$B_0 > \frac{4}{GL} \cdot E. \tag{34}$$

For a number of potential applications, one would need to collect many sets of whole-lung images during a single breath-hold; this will require much stronger gradients—10–20 mT/m—that will create concomitant transverse fields on the order of 10 mT. For diffusion measurements [18], additional diffusion gradients will be needed. To be sensitive to lung microstructure on the alveolar level, diffusion times should not exceed 2–4 ms when the gas molecules remain within a single acinar airway. To achieve the product $bD$ on the order of unity, gradients on the order of 10–20 mT/m are needed for such measurements. These considerations impose the lower limit on $B_0$ of 10–20 mT or higher. Even stronger gradients, hence higher $B_0$ will be needed for really ultra-fast imaging with a sub-second time scale.

In case of fast switching gradients, applied imaging gradients play an "excitation" role similar to RF pulses as local magnetization processes about the tilted field resulting from transverse concomitant components. The net result is that magnetization is tilted from the longitudinal direction toward the transverse plane during the gradient period, Eq. (33). This happens unavoidably throughout the entire object with the effect growing linearly towards the object's edges. At the end of the gradient period, the resultant transverse magnetization (induced by the gradient, not by an RF pulse) will generate spurious signal(s) in the detection coil and could substantially contaminate the desired signal from the targeted region.

During the read-out procedure, when the gradient is on, a time-dependent $z$-component of $\mathbf{M}$ appears in addition to the desired transverse components. Also, an absolute value of the projection of $\mathbf{M}$ on the $XY$-plane becomes time-dependent; hence, a standard interpretation of magnetization rotating in the transverse plane is no longer valid.

One more point should also be mentioned here. Usually, the signal read-out in a positive read-out lobe is preceded by a negative lobe of the gradient to "prewind" spins. This procedure assumes that the concomitant field is absent: when the total magnetic field is solely parallel to the $Z$-axis, the Larmor frequency during the negative and positive lobes differs only by sign (in the rotating frame), and the initial magnetization is restored in the center of read-out interval ($k = 0$). However, in the real case with the unavoidable presence of the concomitant fields this is not so because spins at a given coordinate rotate about *different* axes ($(\tan \beta_\pm = \pm G_x z/(B_0 \pm G_x x))$ with *different* frequencies ($\omega_\pm = \gamma[(B_0 \pm G_x x)^2 + (G_x z)^2]^{1/2}$) during the negative and positive lobes of the gradient. Therefore, the concomitant gradients lead to the magnetization misbalance at the center of $k$-space.

Due to the presence of concomitant gradients all three components of magnetization $\mathbf{M}$ are oscillating with the same spatial-dependent Larmor frequency, Eq. (17), hence all three can be detected simultaneously by specially designed RF coil. Because at very low field, all three components have comparable amplitudes, detection with three orthogonal coils can potentially increase SNR by $\sqrt{3}$ as compared to linear detection and by $\sqrt{3/2}$ as compared to quadrature detection. Though, an actual increase in SNR may be smaller because the magnitude of the oscillating longitudinal magnetization reduces towards the center of FOV.

As described above, the standard frequency-encoding procedure in the presence of the concomitant fields does not provide information about the spin density on planes but rather on cylinders, Eq. (20), or ellipsoids, Eq. (22). This information can also be decoded by back-solving Eqs. (20) and (22). By changing direction of the read-out gradient, the entire space can be covered during the imaging procedure and the 3D image of the object can, in principle, be calculated. This "curve projection reconstruction" approach could enhance opportunities for MRI at very low fields, especially when the adiabatic regime fails. Also, the inhomogeneous orientation of magnetization within the cylindrical or ellipsoidal surfaces would result in inhomogeneous image intensity (apparent spin density) over these surfaces and should be accounted for in the image reconstruction algorithm.

Of course, all the above-mentioned effects are present in conventional and high field imaging (0.1–10 T), however, they are most pronounced in very low field MRI

where they create significant challenges to accurate image reconstruction. New approaches to MRI signal encoding and processing will need to be developed for efficient MRI at very low fields.

## Acknowledgments

The authors are grateful to Professors Mark Conradi and Brian Saam for reading the manuscript and helpful comments. This work is supported in part by NIH Grants R01-NS41519, R01-HL70037, R24-CA83060 (NCI Small Animal Imaging Resource Program (SAIRP)), and P30 CA91842 (NCI Cancer Center Support Program).

## References

[1] W. Happer, Spin exchange, past, present and future, Ann. Phys. Fr. 10 (1985) 645.
[2] M.S. Albert, G.D. Cates, B. Driehuys, W. Happer, B. Saam, C.S. Springer Jr., A. Wishnia, Biological magnetic resonance imaging using laser-polarized 129Xe, Nature 370 (1994) 199.
[3] J.C. Leawoods, D. Yablonskiy, B. Saam, D.S. Gierada, M.S. Conradi, Hyperpolarized $^3$He gas production and MR imaging of the lung, Concepts Magn. Reson. 13 (2001) 277.
[4] H.E. Moller, X.J. Chen, B. Saam, K.D. Hagspiel, G.A. Johnson, T.A. Altes, E.E. de Lange, H.U. Kauczor, MRI of the lungs using hyperpolarized noble gases, Magn. Reson. Med. 47 (2002) 1029.
[5] C.H. Tseng, G.P. Wong, V.R. Pomeroy, R.W. Mair, D.P. Hinton, D. Hoffmann, R.E. Stoner, F.W. Hersman, D.G. Cory, R.L. Walsworth, Low-field MRI of laser polarized noble gas, Phys. Rev. Lett. 81 (1998) 3785.
[6] A.K. Venkatesh, A.X. Zhang, J. Mansour, L. Kubatina, C.H. Oh, G. Blasche, M. Selim Unlu, D. Balamore, F.A. Jolesz, B.B. Goldberg, M.S. Albert, MRI of the lung gas-space at very low-field using hyperpolarized noble gases, Magn. Reson. Imaging 21 (2003) 773.
[7] C.P. Bidinosti, J. Choukeife, P.J. Nacher, G. Tastevin, In vivo NMR of hyperpolarized $^3$He in the human lung at very low magnetic fields, J. Magn. Reson. 162 (2003) 122.
[8] C.P. Bidinosti, J. Choukeife, G. Tastevin, A. Vignaud, P.J. Nacher, MRI of the lung using hyperpolarized $^3$He at very low magnetic field (3 mT), MAGMA 16 (2004) 255.
[9] D.G. Norris, J.M.S. Hutchison, Concomitant magnetic field gradients and their effects on imaging at low magnetic field strengths, Magn. Reson. Imaging 8 (1990) 33.
[10] R.M. Weisskoff, M.S. Cohen, R.R. Rzedzian, Non-axial whole-body instant imaging, Magn. Reson. Med. 29 (1993) 796.
[11] X.J. Zhou, Y.P. Du, M.A. Bernstein, H.G. Reynolds, J.K. Maier, J.A. Polzin, Concomitant magnetic-field-induced artifacts in axial echo planar imaging, Magn. Reson. Med. 39 (1998) 596.
[12] M.A. Bernstein, X.J. Zhou, K.F. King, A. Ganin, N.J. Pelc, G.H. Glover, Concomitant gradient terms in phase contrast MR: analysis and correction, Magn. Reson. Med. 39 (1998) 300.
[13] Y.P. Du, X. Joe Zhou, M.A. Bernstein, Correction of concomitant magnetic field-induced image artifacts in nonaxial echo-planar imaging, Magn. Reson. Med. 48 (2002) 509.
[14] A. Mohoric, J. Stepisnik, M. Kos, G. Planinsic, Self-diffusion imaging by spin echo in earth's magnetic field, J. Magn. Reson. 136 (1999) 22.
[15] S.K. Lee, M. Mobetale, W. Myers, N. Kelso, A.H. Trabesinger, A. Pines, J. Clarke, SQUID-detected MRI at 132 μT with $T(1)$-weighted contrast established at 10 μT–300 mT, Magn. Reson. Med. 53 (2004) 9.
[16] A.N. Matlachov, P.L. Volegov, M.A. Espy, J.S. George, R.H. Kraus, SQUID detected NMR in microTesla magnetic fields, J. Magn. Reson. 170 (2004) 1.
[17] A. Abragam, Principles of Nuclear Magnetism, Oxford University Press, New York, 1989.
[18] D.A. Yablonskiy, A.L. Sukstanskii, J.C. Leawoods, D.S. Gierada, G.L. Bretthorst, S.S. Lefrak, J.D. Cooper, M.S. Conradi, Quantitative in vivo assessment of lung microstructure at the alveolar level with hyperpolarized $^3$He diffusion MRI, Proc. Natl. Acad. Sci. USA 99 (2002) 3111.